





Cross-Scale Energy Transfer From Ion-Scale to Electron-Scale Waves in the Earth's Foreshock Region

Rui Chen^{1,2} , Xinliang Gao^{1,2} , Zhongwei Yang³, Quanming Lu^{1,2} , Zhenyu Kong^{1,2} , Jiuqi Ma^{1,2} , Yangguang Ke^{1,2} , and Chi Wang^{3,4}

¹Deep Space Exploration Laboratory, School of Earth and Space Sciences, University of Science and Technology of China, Hefei, China, ²CAS Center for Excellence in Comparative Planetology, Hefei, China, ³State Key Laboratory of Space Weather, National Space Science Center, Chinese Academy of Sciences, Beijing, China, ⁴College of Earth and Planetary Sciences, University of Chinese Academy of Sciences, Beijing, China

Key Points:

- Using Magnetospheric Multiscale satellite data, we present the evidence of the energy transfer from ion-scale low-frequency fast-magnetosonic waves (LFWs) to electron-scale high-frequency whistler mode waves (HFWs) in the Earth's foreshock region
- Due to the magnetic compression of the LFWs, suprathermal electrons (~10–100s eV) are adiabatically heated in the perpendicular direction
- Both theoretical analysis and observations suggest that the HFWs are excited by those suprathermal electrons through cyclotron resonance

Correspondence to:

X. Gao and Z. Yang,
gaoxl@ustc.edu.cn;
zwyang@swl.ac.cn

Citation:

Chen, R., Gao, X., Yang, Z., Lu, Q., Kong, Z., Ma, J., et al. (2024). Cross-scale energy transfer from ion-scale to electron-scale waves in the Earth's foreshock region. *Journal of Geophysical Research: Space Physics*, 129, e2024JA032567. <https://doi.org/10.1029/2024JA032567>

Received 21 FEB 2024

Accepted 15 JUL 2024

Abstract Cross-scale energy transfer is a fundamental problem in plasma physics but is poorly understood. Based on Magnetospheric Multiscale satellite (MMS) data, we present the evidence of the energy transfer between ion-scale and electron-scale waves in the Earth's foreshock region. Low-frequency fast-magnetosonic waves (LFWs, ~0.2 Hz; ion-gyration scales) are observed in the solar wind upstream of the Earth's bow shock. Due to the magnetic compression of LFWs, suprathermal electrons (~10–100s eV) are adiabatically heated in the perpendicular direction, which leads to the high anisotropy in the high-magnetic-field region. Then high-frequency whistler mode waves (HFWs, 0.1–0.5 f_{ce} ; electron-gyration scales) are excited by those anisotropic electrons through cyclotron resonance. Therefore, this study reveals how energy is transported from LFWs to HFWs, suggesting that wave-particle interactions have played a key role in cross-scale energy transfer in collisionless plasmas.

Plain Language Summary Cross-scale energy transfer is a fundamental problem in plasma physics, in which wave-particle interaction plays an important role. Previous studies provide a limited and incomplete picture of the coupling process between high-frequency whistler mode waves (HFWs, electron-scale) and low-frequency fast-magnetosonic waves (LFWs, ion-scale), and therefore further investigation is still needed to clarify their coupling mechanism. Based on MMS satellite data, we present a promising coupling process between HFWs and LFWs in the Earth's foreshock region. Observation results indicate that suprathermal electrons are perpendicularly heated by the LFWs in the high-magnetic-field region via betatron acceleration. These electrons could generate the HFWs through cyclotron resonance, which is confirmed by both observations and theoretical calculations. Therefore, this event shows the energy transfer among LFWs, suprathermal electrons, and HFWs, illustrating that the energy is directly transported from the ion scale to the electron scale. Our finding provides a potential generation mechanism for HFWs, which may be highly important for understanding the electron dynamics in the Earth's foreshock region.

1. Introduction

The solar-planetary system is filled with a large number of collisionless plasmas, and a variety of physical behaviors occur across multiple scales (Nykyri et al., 2021; Parashar & Matthaeus, 2022; Tu & Marsch, 1995; Verscharen et al., 2019). It spans more than eight orders of magnitude, from the microscopic scales characterized by electron or ion gyro-motions to the macroscopic scales comparable to those of planets (Nykyri et al., 2021; Parashar & Matthaeus, 2022; Tu & Marsch, 1995; Verscharen et al., 2019). Cross-scale energy transfer between these scales is an intriguing and fundamental problem, but the process is poorly understood. Previous studies have indicated that the turbulence cascade model is the most accepted model for cross-scale energy transfer in collisionless plasmas (Alexakis, 2007; Parashar & Matthaeus, 2022; Tu & Marsch, 1995). This model describes the energy transfer from large scales to small scales until it is ultimately dissipated as heat at the molecular scale.

In addition, recent observations have proved that wave-particle interactions play a significant role not only in particle acceleration, precipitation, etc. (Tsurutani et al., 2013; Gao et al., 2023; Kasahara et al., 2018; Kitamura et al., 2018; S. Liu et al., 2015; Ni et al., 2008; Thorne et al., 2010, 2013; Xiao et al., 2009, 2010, 2014; Yuan et al., 2012, 2018), but also in cross-scale energy transfer (Asamura et al., 2021; Z. Liu et al., 2022). Z. Liu et al. (2022) reported that hot ions heated by ultralow-frequency waves transfer energy to electromagnetic ion cyclotron (EMIC) waves and finally dissipate at ion-gyration scales via EMIC-wave induced ion energization.

Asamura et al. (2021) presented an energy transfer process from magnetosonic waves to low-energy protons, during which the transferred energies are further converted to excite EMIC waves. These studies reveal the energy transfer between large scales (e.g., fluid scale) and small scales (e.g., ion-gyration scales) via wave-particle interactions (Asamura et al., 2021; Z. Liu et al., 2022); moreover, the possible coupling process between electron-gyration and ion-gyration scales has also been investigated.

Low-frequency fast-magnetosonic waves (LFWs) usually have a wavelength larger than 1,000 km, comparable with the ion gyro-radii in the Earth's foreshock region (Hobrara et al., 2007; Wang et al., 2021). These waves are an important part of the macroscopic structure upstream of the bow shock and have been widely investigated over the last several decades (Gary et al., 1984; Hobrara et al., 2007; Lu et al., 2024; Tsurutani et al., 1983, 2001; Wang et al., 2020). They are right-hand polarized and typically have the frequencies less than \sim few Hertz, below the lower hybrid resonance frequency (Hobrara et al., 2007; Tsurutani et al., 1983, 2001; Wang et al., 2021). Previous studies have suggested that the generation of LFWs is related to resonant interactions (Gary et al., 1984; Hellinger et al., 2007; Hull et al., 2020; Lu et al., 2024) or nonresonant interactions (Gary et al., 1984; H. Li et al., 2013; Wang et al., 2020, 2021). Moreover, high-frequency whistler mode waves (HFWs, electron-gyration scales), in the frequency range from $\sim 0.1 f_{ce}$ to $0.8 f_{ce}$, have also been detected in the Earth's foreshock region (Artemyev et al., 2022; Bai et al., 2024; Oka et al., 2017; Wang et al., 2020; Yao et al., 2021). Wang et al. (2020) reported the simultaneous observation of HFWs and LFWs, and they speculated that the LFWs may heat electrons and further generate the HFWs, but no direct evidence was provided. Yao et al. (2021) analyzed an observation event in which LFWs could trap electrons in the low-magnetic-field region due to the magnetic mirror force, and those trapped electrons generate HFWs in this region. Bai et al. (2024) reported the observation of HFWs within short large-amplitude magnetic structures (SLAMs) which may evolve from LFWs. These HFWs can be generated by anisotropic electrons that may form during the evolution of SLAMs. Previous studies provided a limited and incomplete picture of the coupling process between HFWs and LFWs (Bai et al., 2024; Wang et al., 2020; Yao et al., 2021), and thus further investigation is still needed to understand the cross-scale energy transfer.

In this study, we present an important coupling process between HFWs and LFWs in the Earth's foreshock region: suprathermal electrons are perpendicularly heated by the LFWs in the high-magnetic-field region via betatron acceleration, and these electrons could provide free energy to generate the HFWs. As a result, the energy is directly transported from the LFWs (ion-gyration scales) to the HFWs (electron-gyration scales). The observations presented here indicate that wave-particle interaction is a potential mechanism for cross-scale energy transfer in collisionless plasmas.

2. Data Sources

The Magnetospheric Multiscale (MMS) mission consists of four identical spacecrafts, and each spacecraft carries a number of plasma and field instruments to measure particle distributions and electromagnetic fields (Burch et al., 2016). In this study, the onboard Fluxgate Magnetometer (FGM, Russell et al., 2016) provides the magnetic field in survey mode (8 or 16 samples/s). The electromagnetic waveform data in burst mode (8,192 samples/s) are measured by the Search Coil Magnetometer (SCM, Le Contel et al., 2016), Axial Double-Probes (ADP, Ergun et al., 2016), and Spin-plane Double-Probes (SDP, Lindqvist et al., 2016). The Fast Plasma Instrument (FPI, Pollock et al., 2016) provides the abundant plasma measurements, including density, velocity, energy spectrum, and pitch angle distribution.

3. Observation Results

On 25 November 2017, all four MMS spacecrafts crossed the Earth's bow shock at $\sim 23:40$ UT from the downstream side (magnetosheath) to the upstream side (solar wind). The spacecraft location during the shock crossing was $[12.8, 5.77, 2.38] R_E$ in the geocentric solar ecliptic (GSE) coordinate system. Figure 1 presents the low-frequency waves and an overview of the shock crossing measured by the MMS-1. The wave frequencies are approximately 0.2 Hz in the spacecraft rest frame according to the wavelet transform analysis (as shown in Figure 1a). Figure 1b shows that the wave magnetic field \vec{B}_w in the frequency range of 0.1–1.0 Hz displays as a series of wave packets, and its magnitude reaches a maximum value close to ~ 5 nT. The background magnetic field \vec{B}_0 (< 0.05 Hz) shown in Figure 1c is used to define the field-aligned coordinate. These waves are observed in the solar wind upstream of the bow shock (as shown in Figures 1d–1i). From the downstream to the upstream,

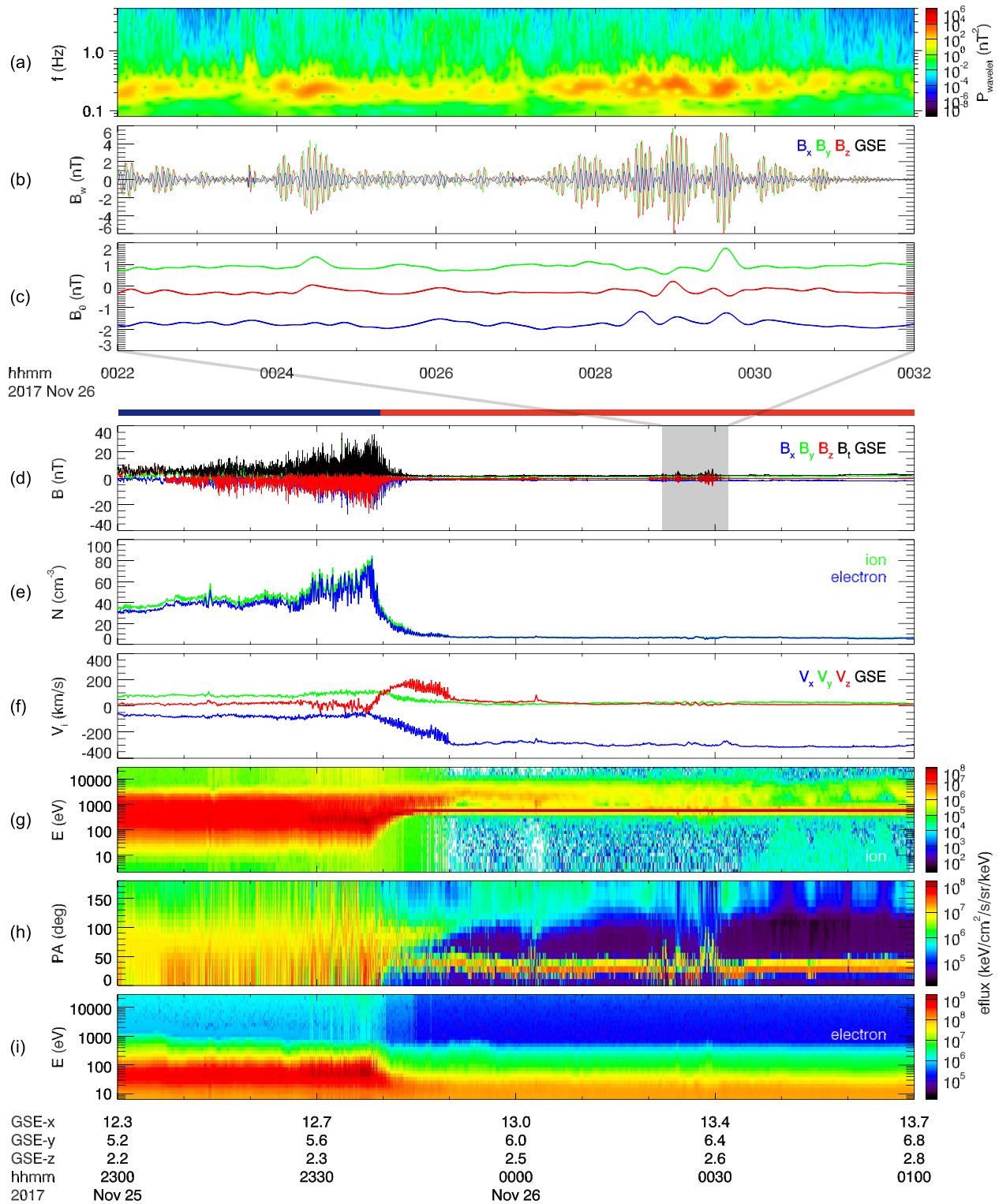


Figure 1. Overview of a shock crossing by MMS-1 on 25 November 2017. (a) Wavelet spectrum based on the magnetic field data measured by FGM, (b) magnetic fields of the low-frequency waves (\vec{B}_w) filtered at 0.1–1.0 Hz, and (c) background magnetic field \vec{B}_0 (<0.05 Hz) at 00:22–00:32 UT; background conditions during the time interval between 11–25/23:00 UT and 11–26/01:00 UT, including (d) magnetic field \vec{B} , (e) electron and ion densities, (f) ion velocity \vec{V}_i , (g) ion energy flux, (h) pitch angle distribution of <30 keV ions, and (i) electron energy flux.

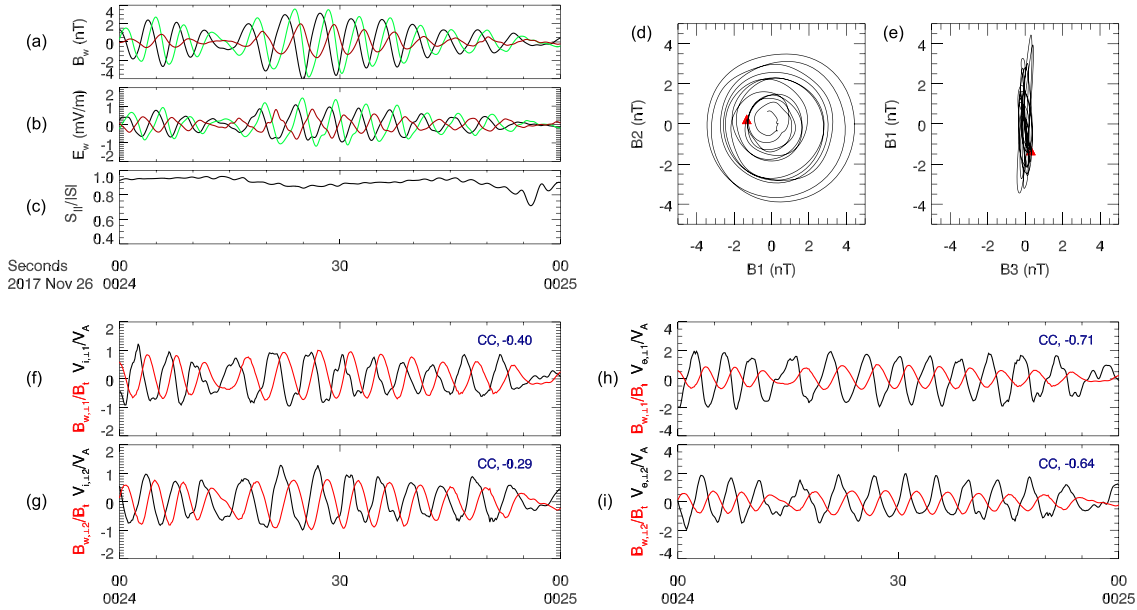


Figure 2. The properties of the low-frequency wave. (a) Wave magnetic fields \vec{B}_w , (b) wave electric fields \vec{E}_w , and (c) the ratio $S_{\parallel}/|S|$, where $|S|$ is the Poynting flux intensity and S_{\parallel} is its parallel component along \vec{B}_0 ; the hodograms for (d) B2–B1 and (e) B1–B3, and (f, g) the perpendicular wave magnetic fields ($B_{w,\perp 1}/B_t$, $B_{w,\perp 2}/B_t$) and ion velocities ($V_{i,\perp 1}/V_A$, $V_{i,\perp 2}/V_A$) filtered at 0.1–1.0 Hz. (h, i) The format is the same as (f, g), but for electron velocities ($V_{e,\perp 1}/V_A$, $V_{e,\perp 2}/V_A$). In panels (d) and (e), B1, B2, and B3 are the magnetic field components in the minimum variance coordinates (B1 is the component along the maximum variance direction, B2 is the component along the intermediate direction, and B3 is the component along the minimum variance direction), and red triangles represent the initial point.

the magnitude of the magnetic field decreases from ~ 10 to ~ 2 nT (Figure 1d), the plasma density decreases from ~ 60 to ~ 10 cm^{-3} (Figure 1e), and the bulk velocity of solar wind increases from ~ 120 km/s to ~ 300 km/s (Figure 1f). Using the mixed mode coplanarity method (Schwartz, 1998), the shock-normal vector \vec{n} is estimated as $[0.919, -0.142, -0.367]$ in GSE, and the shock angle θ_{Bn} is $\sim 57^\circ$. The ion and electron energy fluxes shown in Figures 1g and 1i also indicate that the shock crossing from the magnetosheath (downstream) to the solar wind (upstream). Figure 1h shows the pitch angle distribution of ions with energies less than 30 keV. A reflected ion component (with a pitch angle larger than 100°) can be clearly observed in the solar wind. Therefore, these low-frequency waves are observed in the foreshock region.

To identify the low-frequency wave, we perform further analyses for the magnetic fields during 00:22–00:32 UT, and Figure 2 shows the results for the interval 00:24–00:25 UT (other intervals have similar results). Figures 2a and 2b show the wave magnetic fields \vec{B}_w and electric fields \vec{E}_w in field-aligned coordinates. Then the Poynting vector can be calculated using the formula $\vec{S} = (\vec{E}_w \times \vec{B}_w) / \mu_0$. As shown in Figure 2c, the ratio $S_{\parallel}/|S|$ is positive, indicating that these waves propagate along the background magnetic field \vec{B}_0 . Moreover, the minimum variance analysis (MVA, Sonnerup & Cahill, 1967) is applied. The B2–B1 hodogram in Figure 2d shows the circular polarization of these waves. Here the direction of the background magnetic field points out of the plane; therefore, these waves are right-hand polarized in the spacecraft rest frame. The B1–B3 hodogram in Figure 2e shows that these waves are planar. The MVA result shows that the minimum variance direction is $[-0.943, 0.216, -0.253]$, which is close to the result $(303[-0.945, 0.288, 0.154]$ km/s) based on multi-satellite timing method (Horbury et al., 2002), and then we can obtain that the wave normal angle is $\sim 20^\circ$, which is the angle between the wave phase velocity (i.e., wavevector \vec{k}_{LFW}) and background magnetic field \vec{B}_0 . Figures 2f–2i show the correlation coefficients between the perpendicular magnetic fields $B_{w,\perp}$ and velocities v_{\perp} . The correlation coefficient between $B_{w,\perp 1}/B_t$ and $V_{i,\perp 1}/V_A$ is defined as $CC_{B_{w,\perp 1}, V_{i,\perp 1}}^1$ which is equal to -0.40 (Figure 2f). Figures 2g–2i show that the values of $CC_{B_{w,\perp 1}, V_{i,\perp 1}}^2$, $CC_{B_{w,\perp 1}, V_{e,\perp 1}}^1$, and $CC_{B_{w,\perp 1}, V_{e,\perp 1}}^2$ are -0.29 , -0.71 , and -0.64 , respectively. Based on these features, including propagation direction ($S_{\parallel}/|S| > 0$), phase relation between wave magnetic fields and plasma

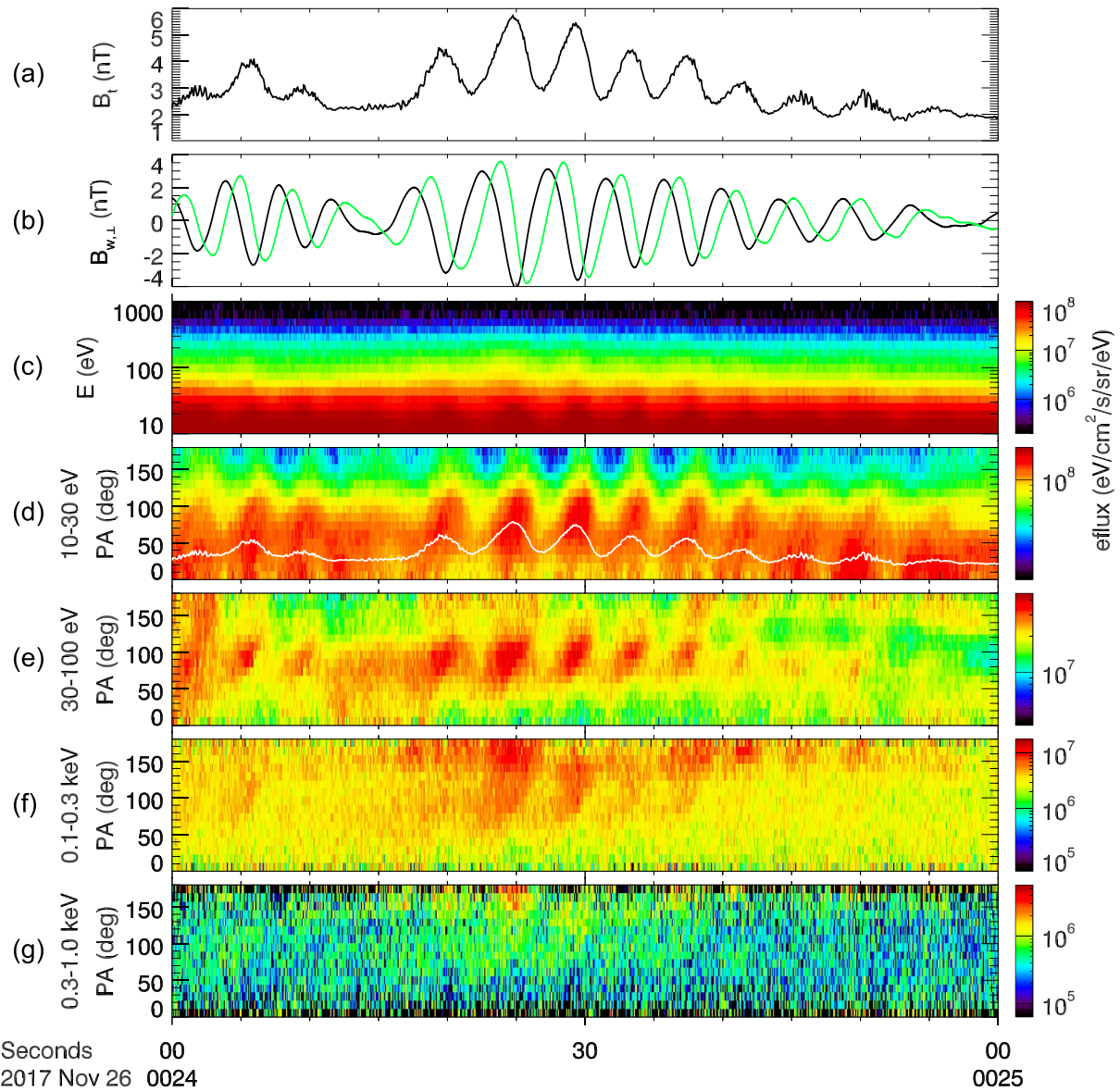


Figure 3. (a) Total magnetic field intensity B_t , (b) perpendicular wave magnetic fields ($B_{w,\perp 1}, B_{w,\perp 2}$), (c) electron energy flux, and (d–g) electron pitch angle distributions in the energy ranges of 10–30 eV, 30–100 eV, 0.1–0.3 keV and 0.3–1.0 keV. In panel (d), white line represents the profile of magnetic intensity.

velocities ($CC_{B_{w,\perp}, V_{\perp}} < 0$), and polarization (right-hand), we can determine that the low-frequency wave is fast-magnetosonic wave (LFW, the detailed identification method can be found in Zhao et al., 2020).

Due to the compression of the LFWs, suprathermal electrons (~ 10 – 100 s eV) are adiabatically heated in the perpendicular direction. Figures 3a and 3b show the magnetic intensity and two perpendicular components (in field-aligned coordinates). The amplitude of the LFWs reaches a maximum value close to 4 nT, which is comparable to the background magnetic field (~ 2 nT), or even larger. Figure 3c shows that the electron energy flux of tens of eV has a larger value (dark red) in the high-magnetic-field region. Then we investigate the electron pitch angle distributions in the energy ranges of 10–30 eV, 30–100 eV, 0.1–0.3 keV and 0.3–1.0 keV (Figures 3d–3g). These electron energy fluxes tend to have larger values in the perpendicular direction, especially in the high-magnetic-field regions. The observational characteristic indicates that these electrons have a larger anisotropy in the high-magnetic field regions.

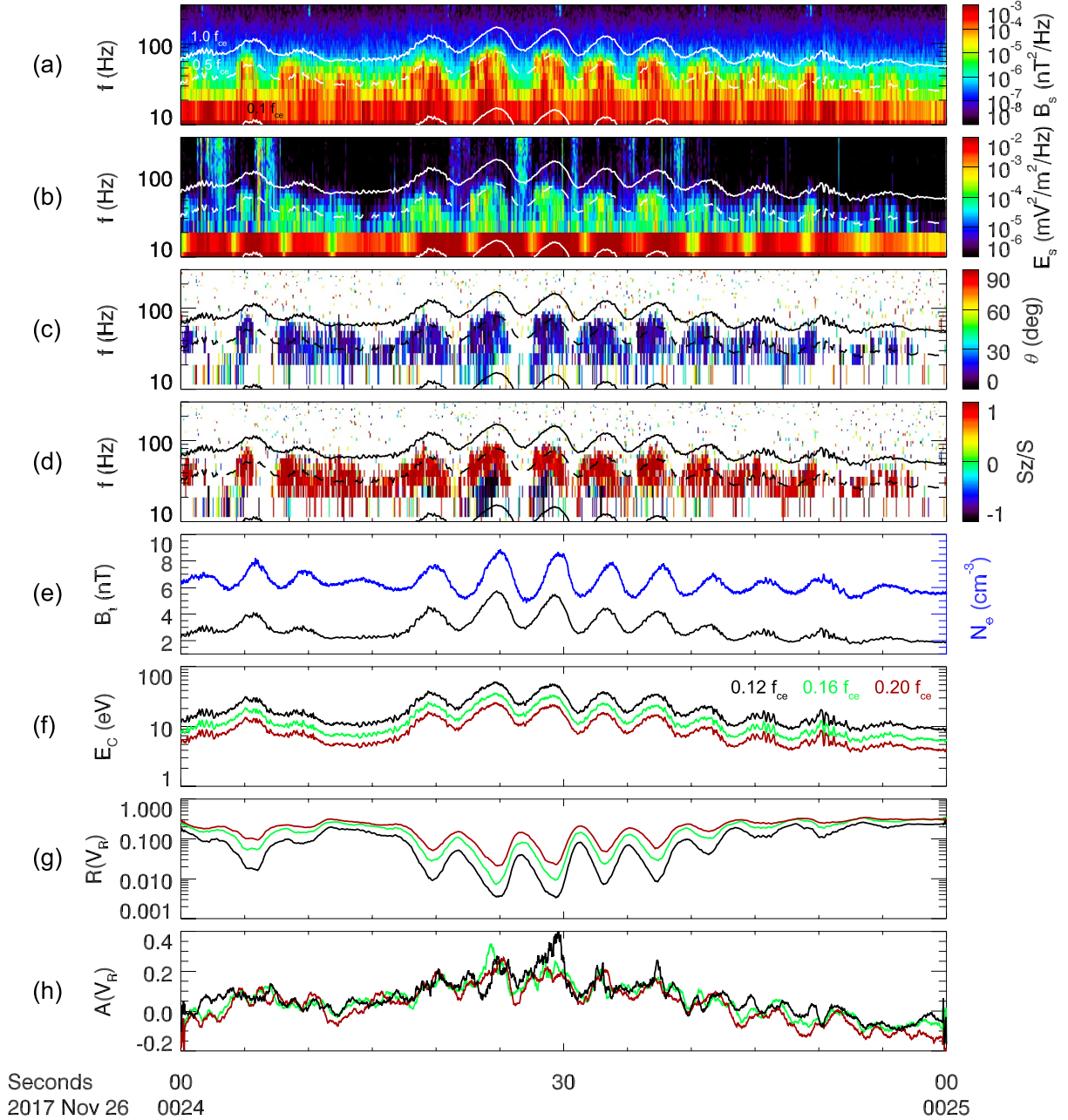


Figure 4. The properties of high-frequency whistler mode waves. (a) Wave magnetic field spectrum, (b) wave electric field spectrum, (c) wave normal angle, (d) the ratio S_z/S , where S is the Poynting flux intensity and S_z is its parallel component along \vec{B} , (e) total magnetic field intensity B_t (black) and electron number density N_e (blue), (f) minimum cyclotron resonance energy of electrons interacting with waves with normalized frequencies of 0.12, 0.16 and 0.20 f_{ce} through the first-order cyclotron resonance, and (g) the ratio of resonant electrons to total electrons $R(V_R)$ and (h) electron anisotropy $A(V_R)$ for wave frequencies of 0.12, 0.16 and 0.20 f_{ce} . The three lines in panels a–d represent 0.1, 0.5, and 1.0 f_{ce} , respectively.

As shown in Figure 4, high-frequency whistler mode waves (HFWs) are simultaneously observed with these thermalized electrons. Figures 4a–4d shows the spectra of the HFWs. These waves are in the frequency range of $\sim 0.1\text{--}0.5 f_{ce}$ ($\sim 10\text{--}80$ Hz), and typically observed in the high-magnetic-field region (Figures 4a and 4b). Figure 4c shows the information of wave normal angle θ , less than 30° . This is the angle between the wavevector \vec{k}_{HFW} and magnetic field \vec{B} , where \vec{B} is the magnetic field shown in Figure 1d, including the background magnetic fields \vec{B}_0 and LFW's magnetic fields \vec{B}_w . Based on the wave electric field and magnetic field data, the propagation

direction is presented in Figure 4d. There are two distinct bands: one propagates along \vec{B} at higher frequencies ($\sim 0.35 f_{ce}$), and the other has opposite propagation directions but lower frequencies ($\sim 0.15 f_{ce}$). Two bands have small wave normal angles, less than 30° (Figure 4c). Here, the bidirectional propagation feature suggests that these waves are observed in the source region, and the small wave normal angles also conform to this conjecture.

In this event, these HFWs are modulated and typically observed in the high-magnetic-field region, which seems to be highly related to the thermalized electrons shown in Figure 3. Figure 4e shows that the variation in the electron density is in phase with the total magnetic field intensity B_T . Assuming that these waves are parallel propagating, the minimum cyclotron resonance energies for three normalized frequencies (0.12, 0.16, and 0.20 f_{ce}) can be determined. The resonance energies are in phase with the total magnetic field intensity B_T . Generally, low magnetic field reduces the cyclotron resonance energy, which leads to more resonant electrons in the low-magnetic-field region. In that frame, whistler mode waves tend to be excited in the low-magnetic-field region (e.g., magnetic equator and minimum B pockets). However, as shown in Figure 4, these HFWs are observed in the high-magnetic-field regions, opposite to the general frame. To investigate the generation of these HFWs, we perform linear theoretical analysis using the method in W. Li et al. (2011). The linear growth rates of parallel-propagating whistler mode waves can be calculated by the following formula,

$$\gamma = \pi |\Omega_{ce}| \cdot R(V_R) \cdot \left[A(V_R) - \frac{1}{|\Omega_{ce}|/\omega - 1} \right], \quad (1)$$

where Ω_{ce} is the electron cyclotron angular frequency, ω is the wave angular frequency, and V_R is the parallel velocity of electrons satisfying the first-order cyclotron resonance condition. $A(V_R)$ is the electron anisotropy for a fixed resonance velocity, and $R(V_R)$ roughly represents the ratio of resonant electrons to total electrons. Since $R(V_R)$ is always positive, the linear growth rate γ is positive when $A(V_R) > \frac{1}{|\Omega_{ce}|/\omega - 1}$. Therefore, whether a whistler mode is unstable depends only on $A(V_R)$, while the rate of growth or damping depends on both $A(V_R)$ and $R(V_R)$. Based on the electron pitch angle distributions measured by FPI instrument, the values of $R(V_R)$ and $A(V_R)$ are presented in Figures 4g and 4h, respectively. The amplitude of the HFWs is strongly inversely correlated with $R(V_R)$ but is correlated with $A(V_R)$. As a result, the electron anisotropy $A(V_R)$, modulated by the LFWs, is the key parameter controlling the generation of these HFWs.

Figures 5a and 5b show the wave magnetic power and the power-weighted average of Sz/S as a function of the normalized frequency ff_{ce} during the interval 00:24:24–00:24:25 UT. There are two distinct bands: one band propagates along \vec{B} with the frequency ranging from $\sim 0.33 f_{ce}$ to $0.45 f_{ce}$ (marked by red shading); the other propagates in the opposite direction with the frequency ranging from $\sim 0.08 f_{ce}$ to $0.2 f_{ce}$ (marked by blue shading). To further verify that the thermalized electrons are responsible for the excitation of HFWs, we calculate the dispersion relation and the linear growth rate using the BO dispersion solver (Xie, 2019). Figure 5c shows the simultaneously measured electron phase space density (in the plasma rest frame) as a function of pitch angle and energy. The observation data is marked by symbols. The electron distribution is obtained by averaging the FPI measurements at 00:24:24–00:24:25 UT. The measured electron distribution shown in Figure 5c is fitted by the sum of drift bi-Maxwellian components as $f = \sum f_i$, $i = 1-5$,

$$f_i = n_i \sqrt{\frac{m}{2\pi T_{\parallel i}}} \frac{m}{2\pi T_{\perp i}} \exp \left[-\frac{m(v_{\parallel} - v_b)^2}{2T_{\parallel i}} - \frac{mv_{\perp}^2}{2T_{\perp i}} \right], \quad (2)$$

where v_{\parallel} and v_{\perp} are the parallel and perpendicular velocities. $T_{\parallel i}$ and $T_{\perp i}$ are the parallel and perpendicular temperatures of the component i , and v_b is its bulk velocity. The number density of each component is represented by n_i . The fitting curves are marked by dotted or solid lines in Figure 5c, and all the fitting parameters are presented in Table 1.

Based on the fitting parameters, we calculate the dispersion relations and linear growth rates shown in Figure 5d, where the red lines represent the calculated waves with parallel propagation direction and the blue lines represent the waves with anti-parallel propagation direction (respect to \vec{B}). The parallel waves have a peak linear growth rate of $\sim 0.0007 \Omega_{ce}$ at the frequency about $0.226 f_{ce}$, and the anti-parallel waves have a peak value of $\sim 0.015 \Omega_{ce}$ at the frequency about $0.217 f_{ce}$. As a result, theoretical analysis indicates that the anti-parallel waves should have

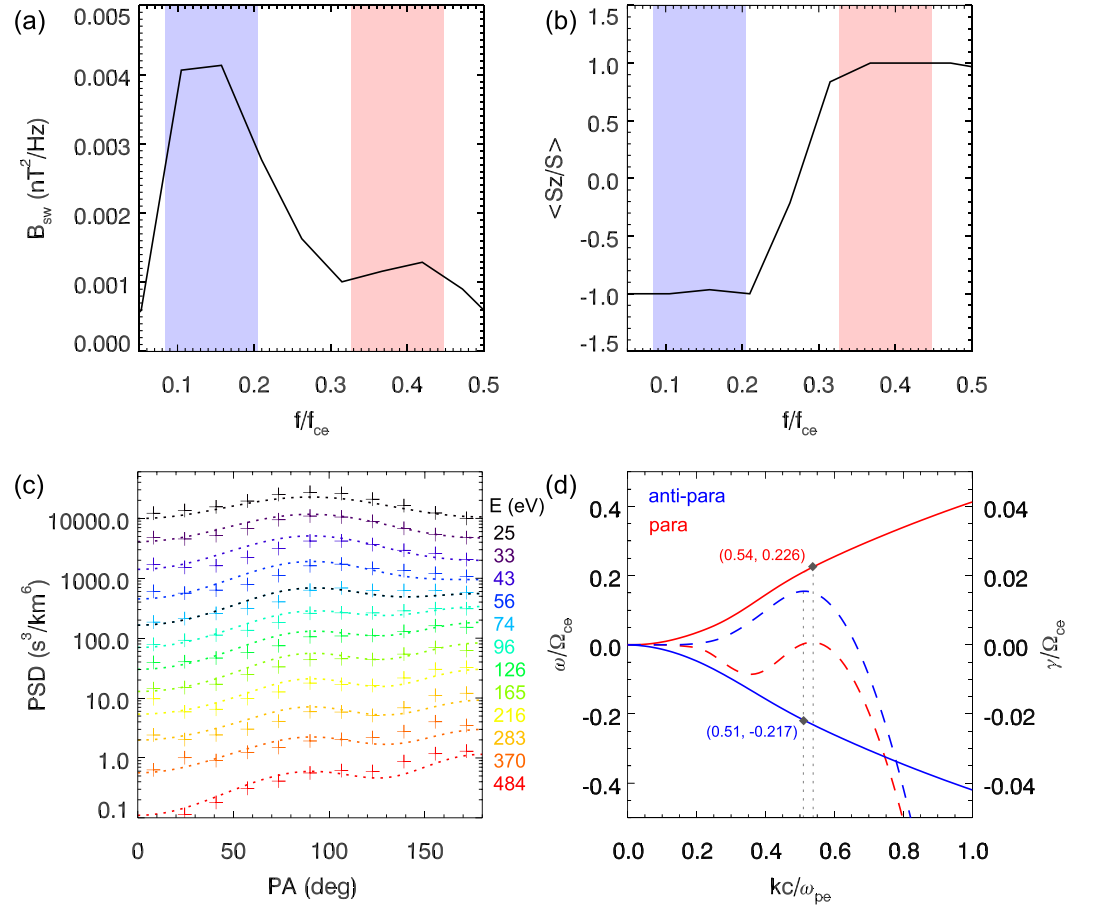


Figure 5. (a) Time integrated power spectral densities of wave magnetic fields B_{sw} , and (b) power-weighted average of Sz/S as a function of normalized frequency f/f_{ce} for the interval 00:24:24–00:24:25 UT; (c) electron phase space densities and their fitted curves as a function of pitch angle and energy, and (d) the dispersion relation and linear growth rate calculated by the BO model, where the red lines represent the calculated waves with parallel propagation direction and the blue lines represent the waves with anti-parallel propagation direction (respect to \vec{B}). In panel (c), observational measurements are represented by symbols, and the fitting curves are represented by lines.

larger amplitudes, which is in good consistent with the observation results shown in Figures 5a and 5b. This event was observed in the solar wind (the bulk velocity is 297.5[−0.995, 0.082, 0.059] km/s in GSE); thus, the Doppler effect caused by the bulk flow needs to be considered. The magnetic field \vec{B} is approximately [−0.297, 0.868, 0.398] in GSE, and the revised frequencies are estimated to be $\sim 0.187f_{ce}$ (anti-parallel) and $\sim 0.256f_{ce}$ (parallel). Therefore, the instability analysis results indicate that there are two sets of waves propagating in opposite directions, which agree well with the observed wave features. In conclusion, these thermalized electrons heated by compressional LFWs can provide free energy for the generation of HFWs.

4. Summary and Discussion

In summary, the observation results reported in this study reveal the energy transfer from LFWs (ion-gyration scales) to HFWs (electron-gyration scales). Due to the magnetic compression of the LFWs, suprathermal electrons (~ 10 – 100 s eV) are adiabatically heated in the perpendicular direction, which leads to the large anisotropy in the high-magnetic-field region. Then the HFWs (0.1 – $0.5f_{ce}$) excited by the anisotropic electrons are simultaneously observed, which is confirmed by the observation and linear instability analysis. Therefore, this study shows the energy transfer among LFWs, suprathermal electrons, and HFWs, illustrating that energy is directly transported from ion-

Table 1
The Fitting Parameters for the Electron Distribution in Figure 5c

$B = 5.54$ nT	n_i (cm^{-3})	T_{\parallel} (eV)	T_{\perp} (eV)	v_b/c
#1	7.515	8	11	0
#2	0.5	24	40	0
#3	0.1	70	92	0
#4	0.13	30	30	−0.00884
#5	0.005	90	90	−0.01977

gyration scales to electron-gyration scales. Our study provides important evidence that wave-particle interactions are a potential mechanism for cross-scale energy transfer in collisionless plasmas.

Simulation and observation studies have suggested that the generation of LFWs is related to resonant interactions (Hellinger et al., 2007; Hull et al., 2020; Lu et al., 2024) or nonresonant interactions (H. Li et al., 2013; Wang et al., 2020). In our event, the obtained wave frequency f is ~ 0.2 Hz, the wave phase velocity v_{ph} is ~ 300 km/s (mainly in the anti-sunward direction, $-\hat{x}$ in GSE), and the wave normal angle is $\sim 20^\circ$. The corresponding wavelength λ (equal to $|v_{ph}|/f$) is $\sim 1,500$ km (comparable with the ion gyro-radii: ~ 797 and $1,128$ km for 0.5 and 1.0 keV protons with pitch angle equal to 30°), and thus the wavenumber is $\sim 0.004189/\text{km}$. Based on the resonant condition ($\omega - \vec{k}_{LFW} \cdot \vec{v}_{res} = n\omega_{ci}, n = \pm 1$), the resulting resonance velocity \vec{v}_{res} is $-270 \hat{x}$ km/s with $n = 1$ and $-369 \hat{x}$ km/s with $n = -1$, which is far from the beam component ($v_{beam,x} = \sim 300$ km/s). Therefore, the conditions are consistent with those of the nonresonant mode, which is similar to the case in Wang et al. (2020).

The electron distributions shown in Figure 3 present two important features: (a) the enhancement of electron fluxes (from ~ 10 to ~ 300 eV) is consistent with the peak of magnetic field intensity; (b) the electron flux has larger values in the perpendicular direction (around 90° pitch angle), especially in the high-magnetic-field region, suggesting the larger anisotropy here. Both features show that these electrons should be heated in the perpendicular direction due to the compression of the low-frequency waves (via betatron acceleration), which is quite different from that in Yao et al. (2021). Yao et al. reported that electrons can be trapped in the low-magnetic-field region (magnetic trough) due to the magnetic mirror force, where the electron fluxes usually peak in the low-magnetic-field region. As a result, our study proposes one different electron-modulating process by LFWs, which is important for the generation of HFWs in the Earth's foreshock region. Moreover, recent study reported the observation of HFWs in SLAMs that may evolve from LFWs (Bai et al., 2024), while our study provides the evidence that HFWs can be generated before the nonlinear evolution of the LFWs.

High-frequency whistler mode waves ($\sim f_{ce}$) are believed to play a significant role in the electron dynamics of Earth's radiation belts (Gao et al., 2023; Kasahara et al., 2018; S. Liu et al., 2015; Ni et al., 2008; Thorne et al., 2010, 2013; Tsurutani et al., 2013; Xiao et al., 2009, 2010, 2014), but their role in the Earth's foreshock remains controversial. Recent studies have suggested that intense HFWs can cause not only electron pitch angle scattering but also electron phase trapping in the foreshock region. Oka et al. (2017) presented evidence that HFWs can efficiently scatter 0.5 – 2 keV electrons by cyclotron resonance. Artemyev et al. (2022) quantified the nonlinear phase trapping of electrons (~ 100 eV) by coherent HFWs, and these electrons are accelerated up to several hundreds of eV. In this study, we show that suprathermal electrons are adiabatically heated in the perpendicular direction by LFWs, and then provide free energy to excite HFWs by cyclotron resonance. Our finding may provide a general picture of the generation of HFWs, which should be highly important for understanding the electron dynamics in the Earth's foreshock region.

Data Availability Statement

The MMS data used in this study are available from the website <https://spdf.gsfc.nasa.gov/pub/data/mms/>. The MMS data analysis is carried out using the publicly available Space Physics Environment Data Analysis System (SPEDAS, <http://spedas.org>).

Acknowledgments

This research was funded by the National Key Research and Development Program of China (No. 2022YFA1604600), the Strategic Priority Research Program of Chinese Academy of Sciences Grant XDB41000000, the NSFC Grant 42322406 and 42230201, the Fundamental Research Funds for the Central Universities, and "USTC Tang Scholar" program. Z. Y. acknowledges the NSFC Grants (42188101, 42150105), the Specialized Research Fund for State Key Laboratories of China, and National Key R&D Program of China No. 2021YFA0718600. We also acknowledge the entire MMS instrument teams.

References

- Alexakis, A. (2007). Nonlocal phenomenology for anisotropic magnetohydrodynamic turbulence. *The Astrophysical Journal*, 667(1), 4–L96. <https://doi.org/10.1086/522048>
- Artemyev, A. V., Shi, X., Liu, T. Z., Zhang, X.-J., Vasko, I., & Angelopoulos, V. (2022). Electron resonant interaction with whistler waves around foreshock transients and the bow shock behind the terminator. *Journal of Geophysical Research: Space Physics*, 127(2), e2021JA029820. <https://doi.org/10.1029/2021JA029820>
- Asamura, K., Shoji, M., Miyoshi, Y., Kasahara, Y., Kasaba, Y., Kumamoto, A., et al. (2021). Cross-energy couplings from magnetosonic waves to electromagnetic ion cyclotron waves through cold ion heating inside the plasmasphere. *Physical Review Letters*, 127(24), 245101. <https://doi.org/10.1103/PhysRevLett.127.245101>
- Bai, S.-C., Shi, Q., Shen, X.-C., Tian, A., Zhang, H., Guo, R., et al. (2024). Whistler mode waves inside short large-amplitude magnetic field Structures: Characteristics and generation mechanisms. *Journal of Geophysical Research: Space Physics*, 129(3), e2023JA032392. <https://doi.org/10.1029/2023JA032392>
- Burch, J. L., Moore, T. E., Torbert, R. B., & Giles, B. L. (2016). Magnetospheric multiscale overview and science objectives. *Space Science Reviews*, 199(1–4), 5–21. <https://doi.org/10.1007/s11214-015-0164-9>

- Ergun, R. E., Tucker, S., Westfall, J., Goodrich, K. A., Malaspina, D. M., Summers, D., et al. (2016). The axial double probe and fields signal processing for the MMS mission. *Space Science Reviews*, 199(1–4), 167–188. <https://doi.org/10.1007/s11214-014-0115-x>
- Gao, X. L., Ma, J. Q., Shao, T., Chen, R., Ke, Y., & Lu, Q. (2023). Why chorus waves are the dominant driver for diffuse auroral precipitation. *Science Bulletin*, 69(5), 597–600. <https://doi.org/10.1016/j.scib.2023.12.009>
- Gary, S. P., Smith, C. W., Lee, M. A., Goldstein, M. L., & Forslund, D. W. (1984). Electromagnetic ion-beam instabilities. *Physics of Fluids*, 27(7), 1852–1862. <https://doi.org/10.1063/1.864797>
- Hellinger, P., Traávníček, P., Lembége, B., & Savoini, P. (2007). Emission of nonlinear whistler waves at the front of perpendicular supercritical shocks: Hybrid versus full particle simulations. *Geophysical Research Letters*, 34(14), L14109. <https://doi.org/10.1029/2007GL030239>
- Hobara, Y., Walker, S. N., Balikhin, M., Pokhotelov, O. A., Dunlop, M., Nilsson, H., & Réme, H. (2007). Characteristics of terrestrial foreshock ULF waves: Cluster observations. *Journal of Geophysical Research*, 112(A7), A07202. <https://doi.org/10.1029/2006JA012142>
- Horbury, T., Cargill, P., Lucek, E., Eastwood, J., Balogh, A., Dunlop, M., et al. (2002). Four spacecraft measurements of the quasiperpendicular terrestrial bow shock: Orientation and motion. *Journal of Geophysical Research*, 107(A8), SSH10-1–SSH10-11. <https://doi.org/10.1029/2001JA000273>
- Hull, A. J., Muschietti, L., Le Contel, O., Dorelli, J. C., & Lindqvist, P.-A. (2020). MMS observations of intense whistler waves within Earth's supercritical bow shock: Source mechanism and impact on shock structure and plasma transport. *Journal of Geophysical Research: Space Physics*, 125(7), e2019JA027290. <https://doi.org/10.1029/2019JA027290>
- Kasahara, S., Miyoshi, Y., Yokota, S., Mitani, T., Kasahara, Y., Matsuda, S., et al. (2018). Pulsating aurora from electron scattering by chorus waves. *Nature*, 554(7692), 337–340. <https://doi.org/10.1038/nature25505>
- Kitamura, N., Kitahara, M., Shoji, M., Miyoshi, Y., Hasegawa, H., Nakamura, S., et al. (2018). Direct measurements of two-way wave-particle energy transfer in a collisionless space plasma. *Science*, 361(6406), 4–1003. <https://doi.org/10.1126/science.aap8730>
- Le Contel, O., Leroy, P., Roux, A., Coillot, C., Alison, D., Bouabdellah, A., et al. (2016). The search-coil magnetometer for MMS. *Space Science Reviews*, 199(1–4), 257–282. <https://doi.org/10.1007/s11214-014-0096-9>
- Li, H., Pang, Y., Huang, S., Zhou, M., Deng, X., Yuan, Z., et al. (2013). The turbulence evolution in the high β region of the Earth's foreshock. *Journal of Geophysical Research: Space Physics*, 118(11), 7151–7159. <https://doi.org/10.1002/2013JA019424>
- Li, W., Thorne, R. M., Bortnik, J., Nishimura, Y., & Angelopoulos, V. (2011). Modulation of whistler mode chorus waves: 1. Role of compressional Pc4-5 pulsations. *Journal of Geophysical Research*, 116(A6), A06205. <https://doi.org/10.1029/2010JA016312>
- Lindqvist, P.-A., Olsson, G., Torbert, R. B., King, B., Granoff, M., Rau, D., et al. (2016). The spin-plane double probe electric field instrument for MMS. *Space Science Reviews*, 199(1–4), 137–165. <https://doi.org/10.1007/s11214-014-0116-9>
- Liu, S., Xiao, F. L., Yang, C., He, Y., Zhou, Q., Kletzing, C. A., et al. (2015). Van Allen Probes observations linking radiation belt electrons to chorus waves during 2014 multiple storms. *Journal of Geophysical Research: Space Physics*, 120(2), 938–948. <https://doi.org/10.1002/2014JA020781>
- Liu, Z. Y., Zong, Q. G., Rankin, R., Zhang, H., Wang, Y. F., Zhou, X. Z., et al. (2022). Simultaneous macroscale and microscale wave-ion interaction in near-earth space plasmas. *Nature Communications*, 13(1), 5593. <https://doi.org/10.1038/s41467-022-33298-6>
- Lu, Q. M., Guo, A., Yang, Z. W., Wang, R., Lu, S., Chen, R., & Gao, X. (2024). Upstream plasma waves and downstream magnetic reconnection at a reforming quasi-parallel shock. *The Astrophysical Journal*, 964(1), 33. <https://doi.org/10.3847/1538-4357/ad2456>
- Ni, B., Thorne, R. M., Shprits, Y. Y., & Bortnik, J. (2008). Resonant scattering of plasma sheet electrons by whistler-mode chorus: Contribution to diffuse auroral precipitation. *Geophysical Research Letters*, 35(11), L11106. <https://doi.org/10.1029/2008GL034032>
- Nykyri, K., Ma, X., & Johnson, J. (2021). Cross-scale energy transport in space plasmas: Applications to the magnetopause boundary. *Magnetospheres in the Solar System*, 109–121. <https://doi.org/10.1002/9781119815624.ch7>
- Oka, M., Wilson, L. B., Phan, T. D., Hull, A. J., Amano, T., Hoshino, M., et al. (2017). Electron scattering by high-frequency whistler waves at Earth's bow shock. *The Astrophysical Journal*, 842(2), L11. <https://doi.org/10.3847/2041-8213/aa7759>
- Parashar, T. N., & Matthaeus, W. H. (2022). Observations of cross scale energy transfer in the inner heliosphere by Parker Solar Probe. *Reviews of Modern Plasma Physics*, 6(1), 41. <https://doi.org/10.1007/s41614-022-00097-x>
- Pollock, C., Moore, T., Jacques, A., Burch, J., Gliese, U., Saito, Y., et al. (2016). Fast plasma investigation for magnetospheric multiscale. *Space Science Reviews*, 199(1), 331–406. <https://doi.org/10.1007/s11214-016-0245-4>
- Russell, C. T., Anderson, B. J., Baumjohann, W., Bromund, K. R., Dearborn, D., Fischer, D., et al. (2016). The magnetospheric multiscale magnetometers. *Space Science Reviews*, 199(1–4), 189–256. <https://doi.org/10.1007/s11214-014-0057-3>
- Schwartz, S. J. (1998). Analysis methods for multi-spacecraft data. *ISSI Scientific Reports Series*, 1, 249.
- Sonnerup, B. U., & Cahill, L. J., Jr. (1967). Magnetopause structure and attitude from Explorer 12 observations. *Journal of Geophysical Research*, 72(1), 171–183. <https://doi.org/10.1029/JZ072i001p00171>
- Thorne, R. M., Li, W., Ni, B., Ma, Q., Bortnik, J., Chen, L., et al. (2013). Rapid local acceleration of relativistic radiation-belt electrons by magnetospheric chorus. *Nature*, 504(7480), 411–414. <https://doi.org/10.1038/nature12889>
- Thorne, R. M., Ni, B., Tao, X., Horne, R. B., & Meredith, N. P. (2010). Scattering by chorus waves as the dominant cause of diffuse auroral precipitation. *Nature*, 467(7318), 944–946. <https://doi.org/10.1038/nature09467>
- Tsurutani, B. T., Lakhina, G. S., & Verkhoglyadova, O. P. (2013). Energetic electron (>10 keV) microburst precipitation. ~5–15 s X-ray pulsations, chorus and wave-particle interactions: A review. *Journal of Geophysical Research: Space Physics*, 118(5), 2296–2312. <https://doi.org/10.1002/jgra.50264>
- Tsurutani, B. T., Smith, E. J., Burton, M. E., Arballo, J. K., Galvan, C., Zhou, X., et al. (2001). Oblique "1-Hz" whistler mode waves in an electron foreshock: The Cassini near-Earth encounter. *Journal of Geophysical Research*, 106(A12), 30223–30238. <https://doi.org/10.1029/2001JA900108>
- Tsurutani, B. T., Smith, E. J., & Jones, D. E. (1983). Waves observed upstream of interplanetary shocks. *Journal of Geophysical Research*, 88(A7), 5645–5656. <https://doi.org/10.1029/ja088ia07p05645>
- Tu, C. Y., & Marsch, E. (1995). MHD structures, waves and turbulence in the solar wind: Observations and theories. *Space Science Reviews*, 73(1–2), 1–210. <https://doi.org/10.1007/BF00748891>
- Verscharen, D., Klein, K. G., & Maruca, B. A. (2019). The multi-scale nature of the solar wind. *Living Reviews in Solar Physics*, 16(1), 5. <https://doi.org/10.1007/s41116-019-0021-0>
- Wang, S., Chen, L.-J., Ng, J., Bessho, N., Le, G., Fung, S. F., et al. (2020). A case study of nonresonant mode 3-s ULF waves observed by MMS. *Journal of Geophysical Research: Space Physics*, 125(11), e2020JA028557. <https://doi.org/10.1029/2020JA028557>
- Wang, S., Chen, L. J., Ng, J., Bessho, N., Le, G., Fung, S. F., et al. (2021). A statistical study of three-second foreshock ULF waves observed by the Magnetospheric Multiscale mission. *Physics of Plasmas*, 28(8), 082901. <https://doi.org/10.1063/5.0055972>
- Xiao, F., Su, Z., Zheng, H., & Wang, S. (2009). Modeling of outer radiation belt electrons by multidimensional diffusion process. *Journal of Geophysical Research*, 114(A3), A03201. <https://doi.org/10.1029/2008JA013580>

- Xiao, F., Su, Z., Zheng, H., & Wang, S. (2010). Three-dimensional simulations of outer radiation belt electron dynamics including cross-diffusion terms. *Journal of Geophysical Research*, *115*(A5), A05216. <https://doi.org/10.1029/2009JA014541>
- Xiao, F., Yang, C., He, Z., Su, Z., Zhou, Q., He, Y., et al. (2014). Chorus acceleration of radiation belt relativistic electrons during march 2013 geomagnetic storm. *Journal of Geophysical Research: Space Physics*, *119*(5), 3325–3332. <https://doi.org/10.1002/2014JA019822>
- Xie, H. (2019). BO: A unified tool for plasma waves and instabilities analysis. *Computer Physics Communications*, *244*, 343–371. <https://doi.org/10.1016/j.cpc.2019.06.014>
- Yao, S. T., Shi, Q. Q., Zong, Q. G., Degeling, A. W., Guo, R. L., Li, L., et al. (2021). Low-frequency Whistler waves modulate electrons and generate higher-frequency Whistler waves in the solar wind. *The Astrophysical Journal*, *923*(2), 216. <https://doi.org/10.3847/1538-4357/ac2e97>
- Yuan, Z., Liu, K., Yu, X., Yao, F., Huang, S., Wang, D., & Ouyang, Z. (2018). Precipitation of radiation belt electrons by EMIC waves with conjugated observations of NOAA and Van Allen satellites. *Geophysical Research Letters*, *45*(23), 12694–12702. <https://doi.org/10.1029/2018GL080481>
- Yuan, Z., Xiong, Y., Pang, Y., Zhou, M., Deng, X., Trotignon, J. G., et al. (2012). Wave-particle interaction in a plasmaspheric plume observed by a Cluster satellite. *Journal of Geophysical Research*, *117*(A3), A03205. <https://doi.org/10.1029/2011JA017152>
- Zhao, J., Wang, T., Graham, D. B., He, J., Liu, W., Dunlop, M. W., & Wu, D. (2020). Identification of the nature of electromagnetic waves near the proton-cyclotron frequency in solar-terrestrial plasmas. *The Astrophysical Journal*, *890*(1), 17. <https://doi.org/10.3847/1538-4357/ab672f>